Neutrinos from Beta Processes in a Presupernova

Probing the Isotopic Evolution of a Massive Star

Patton, K.M.; Lunardini, C.; Farmer, R.J.; Timmes, F.X.

Link to publication

Neutrinos from Beta Processes in a Presupernova: Probing the Isotopic Evolution of a Massive Star

Kelly M. Patton[1] , Cecilia Lunardini[2] , Robert J. Farmer[3,4] , and F. X. Timmes[4,5]

[1] Institute for Nuclear Theory, University of Washington, Seattle, WA 98195 USA; kmpatton@uw.edu
[2] Department of Physics, Arizona State University, Tempe, AZ 85287-1504 USA; cecilia.lunardini@asu.edu
[3] Anton Pannenkoek Institute for Astronomy, University of Amsterdam, NL-1090 GE Amsterdam, The Netherlands; r.j.farmer@uva.nl
[4] School of Earth and Space Exploration, Arizona State University, Tempe, AZ 85287-1504 USA
[5] JINA, Joint Institute for Nuclear Astrophysics, USA; ftimmes@asu.edu

Abstract

We present a new calculation of the neutrino flux received at Earth from a massive star in the $\sim$24 hr of evolution prior to its explosion as a supernova (presupernova). Using the stellar evolution code MESA, the neutrino emissivity in each flavor is calculated at many radial zones and time steps. In addition to thermal processes, neutrino production via beta processes is modeled in detail, using a network of 204 isotopes. We find that the total produced ν_e flux has a high-energy spectrum tail, at $E \gtrsim$ 3–4 MeV, which is mostly due to decay and electron capture on isotopes with $A = 50$–60. In a tentative window of observability of $E \gtrsim 0.5$ MeV and $t < 2$ hr pre-collapse, the contribution of beta processes to the ν_e flux is at the level of $\sim$90%. For a star at $D = 1$ kpc distance, a 17 kt liquid scintillator detector would typically observe several tens of events from a presupernova, of which up to $\sim$30% is due to beta processes. These processes dominate the signal at a liquid argon detector, thus greatly enhancing its sensitivity to a presupernova.

Key words: astroparticle physics – neutrinos

1. Introduction

The advanced evolution of massive stars—which culminates in their collapse, and possible explosion as supernovae—has been observed so far only in the electromagnetic band. Completely different messengers, the neutrinos, dominate the star's energy loss from the core carbon-burning phase onward, and with their fast diffusion timescale, they set the very rapid pace (from months to hours) of the latest stages of nuclear fusion (presupernova). These neutrinos have never been detected; their observation in the future would offer a unique and direct probe of the physical processes that lead to stellar core collapse.

In a star's interior, neutrinos are produced via a number of thermal processes—mostly pair production—and via β-processes, i.e., electron/positron captures on nuclei and nuclear decay. The neutrino flux from thermal processes mainly depends on the thermodynamic conditions in the core. The neutrino flux from β reactions has a stronger dependence on the isotopic composition, and thus on the complex network of nuclear reactions that take place in the star. In this respect, the two classes of production, thermal and β, carry complementary information.

At this time, the study of the thermal neutrino flux from a presupernova star is fairly mature. Exploratory studies in 2003–2010 (Odrzywolek et al. 2004a, 2004b; Kutschera et al. 2009; Odrzywolek & Heger 2010) showed that they can be detected in the largest neutrino detectors for a star at a distance $D \lesssim 1$ kpc. Later, detailed descriptions of the thermal processes (Ratkovic et al. 2003; Dutta et al. 2004; Misiaszek et al. 2006; Odrzywolek 2007) have been applied to state-of-the-art numerical simulations of stellar evolution, to obtain the time-dependent presupernova neutrino flux expected at Earth (Kato et al. 2015; Yoshida et al. 2016). The potential of presupernova neutrinos as an early warning of an imminent nearby supernova was emphasized (Yoshida et al. 2016).

For the neutrinos from β processes (henceforth βp), the status is very different. Dedicated studies have developed much more slowly, as it was recognized early on (Odrzywolek 2009; Odrzywolek & Heger 2010) that they required a complex numerical study of realistic stellar models with large nuclear networks.

In a recent publication (Patton et al. 2017), we have approached the challenge of modeling the βp in detail—in addition to the thermal processes—for a realistic, time-evolving star simulated with the MESA software instrument (Paxton et al. 2011, 2013, 2015). The 204 isotope nuclear network of MESA, fully coupled to the hydrodynamics during the entire calculation, made it possible to obtain, for the first time, consistent and detailed emissivities and energy spectra for the β neutrinos, at sample points inside the star at selected times pre-collapse. It was found that βp contribute strongly to the total neutrino emissivities, and even dominate at late times and in the energy window relevant for detection ($E \gtrsim 2$ MeV or so). Using an independent numerical simulation, with a combination of nuclear network and arguments of statistical equilibrium, Kato et al. (2017) reached similar conclusions, and calculated the rates of events expected in neutrino detectors as a function of time as well as total numbers of events.

In this paper, we further extend the study of presupernova neutrinos, with an emphasis on a realistic, consistent description of the flux from βp. For two progenitor stars, evolved with MESA, the time-dependent neutrino emissivities for different production processes are integrated over the volume of emission, to obtain the neutrino luminosities and energy spectra expected at Earth for each neutrino flavor. For several time steps leading to the collapse, the isotopes that dominate the βp emission, for both neutrinos and anti-neutrinos, are identified. We discuss the prospects of detectability, and how they depend on the distance to the star, ranging from the nearby Betelgeuse to progenitors as far as the horizon of detectability,

beyond which no observable signal is expected. In the discussion, the main guaranteed detector backgrounds are taken into account.

The paper is structured as follows. In Section 2, a concise summary of our simulation is given. Section 3 gives the results for the neutrino flux and energy spectrum produced in a presupernova star as a function of the time, pre-collapse. Section 4 shows the expected neutrino flux at Earth, with a brief discussion of oscillation effects and detectability. A discussion follows in Section 5.

2. Neutrino Production and Stellar Evolution

We simulate the evolution of two stars of initial masses $M = 15, 30\ M_\odot$ (with $M_\odot$ being the mass of the Sun), from the pre-main-sequence phase to core collapse, using MESA r7624 (Paxton et al. 2011, 2013, 2015), for which in lists and stellar models used are publicly available.[6] The MESA runs used here are the same as those in Farmer et al. (2016), where technical details can be found. Each star is modeled as a single, non-rotating, non-mass-losing, solar metallicity object. The calculation stops at the onset of core collapse, which is defined as the time when any part of the star exceeds an infall velocity of 1000 km s^{-1}. We also set the maximum mass of a grid zone to be $\Delta M_{\max} = 0.1\ M_\odot$. The simulations employ a large, in situ, nuclear reaction network, `mesa_204.net`, consisting of 204 isotopes up to ^{66}Zn, and including all relevant reactions. They also include the effects of convective overshoot, semi-convection, and thermohaline-mixing on the chemical mixing inside the star.

In output, MESA gives the time- and space-profiles of the temperature T, matter density ρ, isotopic composition, and electron fraction Y_e. These quantities are then used in a separate calculation to derive the neutrino fluxes, as outlined in our previous work (Patton et al. 2017). For brevity, here, only the main elements are summarized.

We calculate the spectra for ν_e, $\bar{\nu}_e$, and ν_μ, ν_τ, $\bar{\nu}_\mu$, $\bar{\nu}_\tau$ (collectively called ν_x and $\bar{\nu}_x$ from here on) resulting from β processes and pair annihilation. Other thermal processes (Patton et al. 2017) were found to be by far subdominant in the late-time neutrino emission from the whole star, and were neglected for simplicity.

In the calculation of spectra for the βp, the relevant rates are taken from the nuclear tables of Fuller, Fowler, and Newman (FFN; Fuller et al. 1980, 1982a, 1982b, 1985), Oda et al. (OEA; Oda et al. 1994) and Langanke and Martinez-Pinedo (LMP; Langanke et al. 2001). For isotopes that appear in multiple tables, the rates of LMP are given precedence, followed by OEA, then finally FFN. This order of precedence is the same as that used in MESA (Paxton et al. 2011).

As described in FFN (Fuller et al. 1980, 1982a, 1982b, 1985), the rate of decay from a parent nucleus in the excited state i to a daughter in excited state j is

$$\lambda_{ij} = \log 2\, \frac{f_{ij}(T, \rho, \mu)}{\langle ft \rangle_{ij}}. \tag{1}$$

Here, $\langle ft \rangle_{ij}$ is the comparative half-life, containing all of the nuclear structure information and the weak interaction matrix element. The function f_{ij} is the phase space of the incoming and

outgoing electrons or positrons. It uniquely determines the shape of the resulting neutrino spectrum, because the outgoing neutrinos are presumed to be free-streaming with no Pauli blocking.

Since the shape of the spectrum is entirely determined by the phase space, we can define the spectrum as $\phi = N f_{ij}(T, \rho, \mu)$, where N is a normalization factor. We then write the spectra for the βp neutrinos for a single isotope as

$$\phi_{\mathrm{EC,PC}} = N\frac{E_\nu^2(E_\nu - Q_{ij})^2}{1 + \exp((E_\nu - Q_{ij} - \mu_e)/kT)}\Theta(E_\nu - Q_{ij} - m_e) \tag{2}$$

$$\phi_\beta = N\frac{E_\nu^2(Q_{ij} - E_\nu)^2}{1 + \exp((E_\nu - Q_{ij} + \mu_e)/kT)}\Theta(Q_{ij} - m_e - E_\nu), \tag{3}$$

where EC (PC) is for electron (positron) capture, and β is for decay. The chemical potential μ_e is defined to include the rest mass such that $\mu_{e^-} = -\mu_{e^+}$. The parameter $Q_{ij} = M_p - M_d + E_i - E_j$ is the Q-value for the transition, where $M_{p,d}$ is the mass of the parent (daughter) and $E_{i,j}$ is the excitation energy.

The rates reported in the FFN, OEA, and LMP tables are actually the sum of all possible transitions, so $\lambda = \Sigma \lambda_{ij}$. So rather than finding individual values for each Q_{ij}, we follow the method of Langanke et al. (2001) and Patton et al. (2017), and instead find an effective Q-value. We calculate the spectrum and its average energy, then adjust the Q-value until the average energy in the rate tables is reproduced. Note that the tabulated average energy is a combined value for both decay and capture, therefore Q is the same for both processes.

The parameter N in Equations (2)–(3) is a normalization factor, defined to reproduce the tabulated rates λ_i for isotope i:

$$\lambda_i = \int_0^\infty \phi_i dE_\nu \quad i = \mathrm{EC, PC}, \beta^\pm. \tag{4}$$

The total spectrum of neutrinos from βp (comprehensive of both capture and decay processes) is given by the sum over all the isotopes, weighed by their abundances X_k:

$$\left(\frac{dR_\beta}{dE}\right)_{\nu_e, \bar{\nu}_e} = \sum_k X_k \phi_k \frac{\rho}{m_p A_k}. \tag{5}$$

Here, m_p is the mass of the proton, and A_k is the atomic number of the isotope k.

For neutrinos produced via pair annihilation, the emission rate, differential in the neutrino energy, is

$$\left(\frac{dR}{dE}\right)_{\nu_\alpha, \bar{\nu}_\alpha} = \int d^3p_1 d^3p_2 \left(\frac{d\sigma v}{dE}\right)_{\nu_\alpha, \bar{\nu}_\alpha} f_1 f_2, \tag{6}$$

where f_i is the Fermi–Dirac distribution function for the electron and positron, and

$$d\sigma\, v = \frac{1}{2\mathcal{E}_1}\frac{1}{2\mathcal{E}_2}\frac{1}{(2\pi)^2}\delta^4(P_1 + P_2 - Q_1 - Q_2)$$
$$\times \frac{d^3q_1}{2E_1}\frac{d^3q_2}{2E_2}\langle|\mathcal{M}|^2\rangle. \tag{7}$$

Here, v is the relative velocity of the electron-positron pair, $P_{1,2} = (\mathcal{E}_{1,2}, \boldsymbol{p}_{1,2})$ is the four-momentum of the electron (positron), and $Q_{1,2} = (E_{1,2}, \boldsymbol{q}_{1,2})$ is the four-momentum of the

(anti-)neutrino. The squared matrix element, as given by Misiaszek et al. (2006), is

$$\langle|\mathcal{M}|^2\rangle = 8G_F^2((C_A^f - C_V^f)^2(P_1 \cdot Q_1)(P_2 \cdot Q_2)$$
$$+ (C_A^f + C_V^f)^2(P_2 \cdot Q_1)(P_1 \cdot Q_2)$$
$$+ m_e^2(C_V^2 - C_A^2)(Q_1 \cdot Q_1)). \qquad (8)$$

Here, $C_V^e = 1/2 + 2\sin^2\theta_W$, $C_A^e = 1/2$, and $C_{V,A}^x = C_{V,A}^e - 1$.

In Patton et al. (2017), Equations (5) and (6) were used to calculate the spectra for selected times and points inside a star. Here, we integrate over the emission region to obtain the number luminosity—i.e., the number of neutrinos that leave the star per unit time—and the differential luminosity:

$$\frac{dL_N^{\nu_\alpha}}{dE} = 4\pi \int \left(\frac{dR}{dE}\right)_{\nu_\alpha} r^2 dr, \qquad (9)$$

$$L_N^{\nu_\alpha} = \int \frac{dL_N^{\nu_\alpha}}{dE} dE. \qquad (10)$$

3. Results: Time Profiles and Spectra

Results were obtained for discrete times (time-to-collapse, τ_{CC}) between the onset of core oxygen-burning and the onset of core collapse. An interval of two hours prior to collapse—when the chance for detection is greatest—was mapped in greater detail. Specifically, for the 15 $M_\odot$ (30 $M_\odot$) model, we took a total of 21 (26) time instants, of which 15 (20) were in the final two hours. All the calculated times are shown in Figure 1, while a subset of seven times is investigated in more detail in the other figures and tables. The calculations of the numbers of events in the detectors use all the calculated times within the last two hours.

3.1. A Neutrino Narrative: Time-evolving Luminosities

Let us examine the thermal history of the two progenitors, and how it is reflected in the neutrino luminosity. Figure 1 shows the star's trajectory in the plane of central temperature and central density, (T_c, ρ_c), as the time evolves. It also shows the evolution for the neutrino number luminosities, $L_N^{\nu_\alpha}$, for different production channels, and the approximate times of ignition of the various fuels.

From the figure, it appears that the evolution of the two stars is generally similar, the main difference being that the more massive progenitor evolves faster and is overall brighter in neutrinos. In particular, for the 15 $M_\odot$ (30 $M_\odot$) star the burning stages for the two stars proceed as follows: at $\tau_{CC} \approx 10^4$ hr ($\tau_{CC} \approx 10^3$ hr), oxygen ignition takes place in the core, and proceeds convectively until it ceases at $\tau_{CC} \approx 10^3$ hr ($\tau_{CC} \approx 10^2$ hr). Then, an oxygen shell is ignited and burns until $\tau_{CC} \approx 5 \times 10^2$ hr ($\tau_{CC} \approx 10$ hr). Eventually, silicon-burning is ignited in the core and proceeds until $\tau_{CC} \approx 10$ hr ($\tau_{CC} \approx 5$ hr). At that point the star transitions to shell silicon-burning, which proceeds until collapse. Interestingly, the 15 $M_\odot$ star has an intermediate phase (which is absent in the more massive progenitor) before core silicon-burning: a second, off-center oxygen-burning stage, which lasts until $\tau_{CC} \approx 10^2$ hr.

In Figure 1, we can see how the luminosity of ν_e from βp grows faster than those of thermal processes. For the 15 $M_\odot$ (30 $M_\odot$) case, it amounts to $\sim$30% ($\sim$10%) of the contribution from pair annihilation at the onset of oxygen-burning; it

becomes comparable to pair annihilation at $\tau_{CC} \approx 6$ minute ($\tau_{CC} \approx 7$ s), increasing to almost an order of magnitude greater ($\sim$30 times greater) at the onset of core collapse.

The luminosity of $\bar{\nu}_e$ from βp follows a more complicated pattern, tracing more closely the phases of stellar evolution. It drops after core oxygen-burning ends, and begins increasing again after silicon core-ignition. The total $\bar{\nu}_e$ emission is always dominated by pair annihilation, although the disparity decreases as the stars approach core collapse. At the onset of core collapse, the βp contribution is approximately 40% ($\sim$20%) of the pair process for the 15 $M_\odot$ (30 $M_\odot$ model) model.

A unique feature of the 15 $M_\odot$ model is a short sharp drop in the luminosities of all neutrino species, shortly after shell silicon-burning begins, followed by a smooth increase. This peak is absent in the time profiles of the 30 $M_\odot$ model, for which the time profiles are smoother. This difference can be traced to differences in the core carbon-burning phases of the two stars, which proceed convectively for the $M = 15 M_\odot$ case and radiatively for the $M = 30 M_\odot$ model.[7] For convective core C-burning, efficient neutrino emission decreases the entropy. This entropy loss is missing in the radiative carbon-burning case, causing all subsequent burning stages to take place at higher entropy, higher temperatures, and lower densities. In these conditions, density gradients are smaller and extend to larger radii, thus explaining the smoother profiles of the 30 $M_\odot$ model.

We note that the neutrino luminosity from pair annihilation increases more slowly in the last few hours of evolution. This can be understood by considering that the emissivity for pair annihilation is nearly independent of the density for fixed temperature (Itoh et al. 1996), and therefore directly reflects the moderate increase of the temperature (Figure 1, right panels) over hour-long periods.

Generally, the patterns found here are consistent with those in the recent work by Kato et al. (2017). The main difference is in the $\bar{\nu}_e$ luminosity from βp, which in our work is always subdominant, while in Kato et al. it dominates over pair annihilation starting at $\tau_{CC} \sim 0.5$ hr. This discrepancy could be due to the nuclear networks used: in our work, the network mesa_204.net is evolved self-consistently within MESA to obtain mass fractions, and tabulated βp rates from FFN, ODA, and LMP are used (see Section 2 and Patton et al. 2017). Instead, Kato et al. calculate mass fractions using nuclear statistical equilibrium, and incorporate many neutron-rich isotopes, with rates taken from tables by Tachibana and others (Tachibana & Yamada 1995; Tachibana 2000; Yoshida & Tachibana 2000; Koura et al. 2003, 2005), which they adapted to the stellar environment of interest (the original tables are for terrestrial conditions).

3.2. Neutrino Spectra: Isotopic Contributions

Let us now discuss the neutrino energy spectra and the effect of the βp on them. Figure 2 gives the number luminosities, differential in energy, of each neutrino species at seven selected times of the evolution (see Tables 1 and 2 for exact values).

---

[7] The dividing line between the two paths is given by the central carbon-mass fraction, with a critical value $X(^{12}C) \sim 20\%$ (Weaver & Woosley 1993; Timmes et al. 1996; Woosley et al. 2002). For the MESA inputs used here, solar metallicity models with zero-age main-sequence masses below $\simeq 20\,M_\odot$ have $X(^{12}C) \gtrsim 20\%$ and thus undergo convective core carbon-burning. See, e.g., I. Petermann et al. (2017, in preparation).
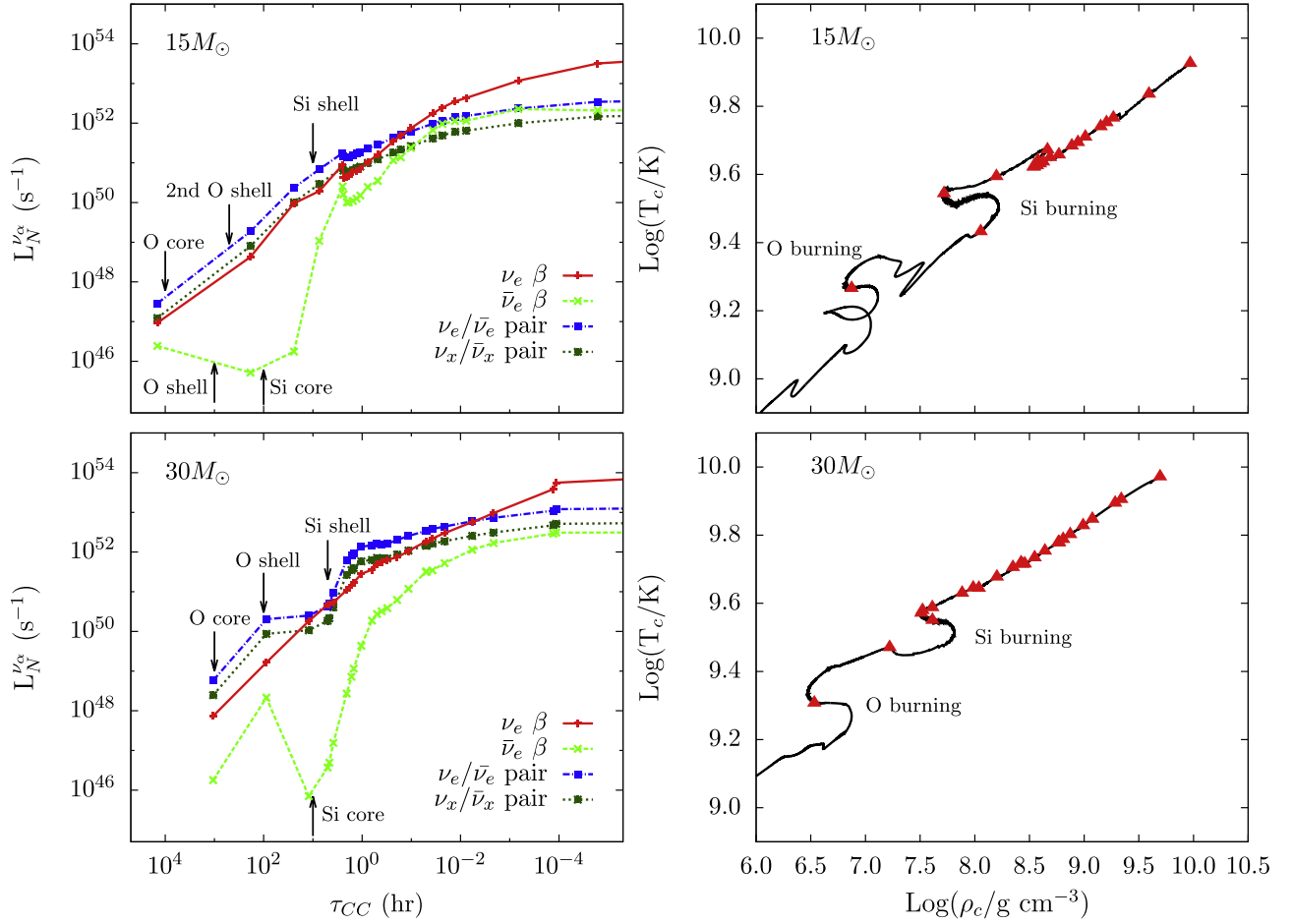
Figure 1. Time evolution of the two progenitors of mass $M = 15, 30\,M_\odot$. Here, τ_{CC} is the time-to-collapse (in hours). In all figures, the markers correspond to the points at which the neutrino luminosities were calculated. Left: total number luminosities for different production channels: ν_e from βp, $\bar{\nu}_e$ from βp, $\nu_e/\bar{\nu}_e$ from pair annihilation, and $\nu_x/\bar{\nu}_x$ from pair annihilation. The arrows indicate approximate times of ignition for the different fuels. Right: the trajectory in the plane of central temperature and central density.

Separate panels show the percentages of the ν_e and $\bar{\nu}_e$ luminosities that originate from βp alone.

We observe that the ν_e and $\bar{\nu}_e$ spectra are smooth at all times, as the integration over the emission volume averages out spectral structures due to βp from individual isotopes, which appear at early times and in certain shells (Patton et al. 2017). The spectra have a maximum at $E \sim 1$–3 MeV depending on the time. At $E \gtrsim 4$ MeV, the ν_e spectrum is dominated by the βp at all times of interest (fraction of βp larger than $\sim 60\%$). At all energies, the βp contribution increases with time, and it exceeds a 90% fraction at collapse in the entire energy interval, consistent with Figure 1.

The percentage of $\bar{\nu}_e$ from βp is lower, overall. Over time, it increases at low energy ($E \lesssim 1$ MeV), reaching a $\sim 50\%$ fraction at $E = 1$ MeV at collapse, and decreases at higher energy. This latter behavior reflects the fact that the electron degeneracy increases with time, thus reducing the phase space for electrons in the final state due to β^- decay. The lower number density of positrons (relative to electrons) available for capture also explains the suppression of the βp $\bar{\nu}_e$ flux relative to ν_e.

A complementary view of these results is given in Figure 3, which shows the time evolution of the neutrino luminosities differential in E, at selected values of E. We see that, for the $15\,M_\odot$ model, the neutrino luminosity from βp has a peak at $\tau_{CC} \approx 2$ hr, followed by a minimum and a subsequent fast

increase. This is the same feature that appears in the total luminosities for the same progenitor (Figure 1), and is more pronounced at higher neutrino energies.

What can we learn from presupernova neutrinos about the isotopic evolution of a star? To start addressing this question, we investigated what nuclear isotopes contribute the most to the ν_e and $\bar{\nu}_e$ fluxes in the detectable region of the spectrum. This is addressed in Tables 1 and 2, where, for selected times in the $\tau_{CC} \lesssim 2$ hr, we list the five strongest contributors to both the total luminosity and the luminosity in the window $E \geqslant 2$ MeV (where detectors are most sensitive; see Section 4.3). The tables also give the fraction of the βp number luminosity that each isotope produces. These tables give us a view into how the isotopic makeup of the star evolves over time.

Let us first describe results for the $15\,M_\odot$ model. In it, silicon shell-burning begins at $\tau_{CC} \approx 10$ hr (Section 3.1). Thus, in the last two hours before collapse, the isotopic composition is already heavy. The top-five dominant isotopes—for both ν_e and $\bar{\nu}_e$ production—are those with $A \approx 50$–60, such as iron, manganese, cobalt, and chromium. At very late times, t_6 and t_7, photodissociation of nuclei becomes efficient, producing free nucleons. We find that free protons are the strongest contributor to the ν_e luminosity at those times.

By summing the contributions listed in Table 1, we see that the five dominant isotopes are producing a large percentage of
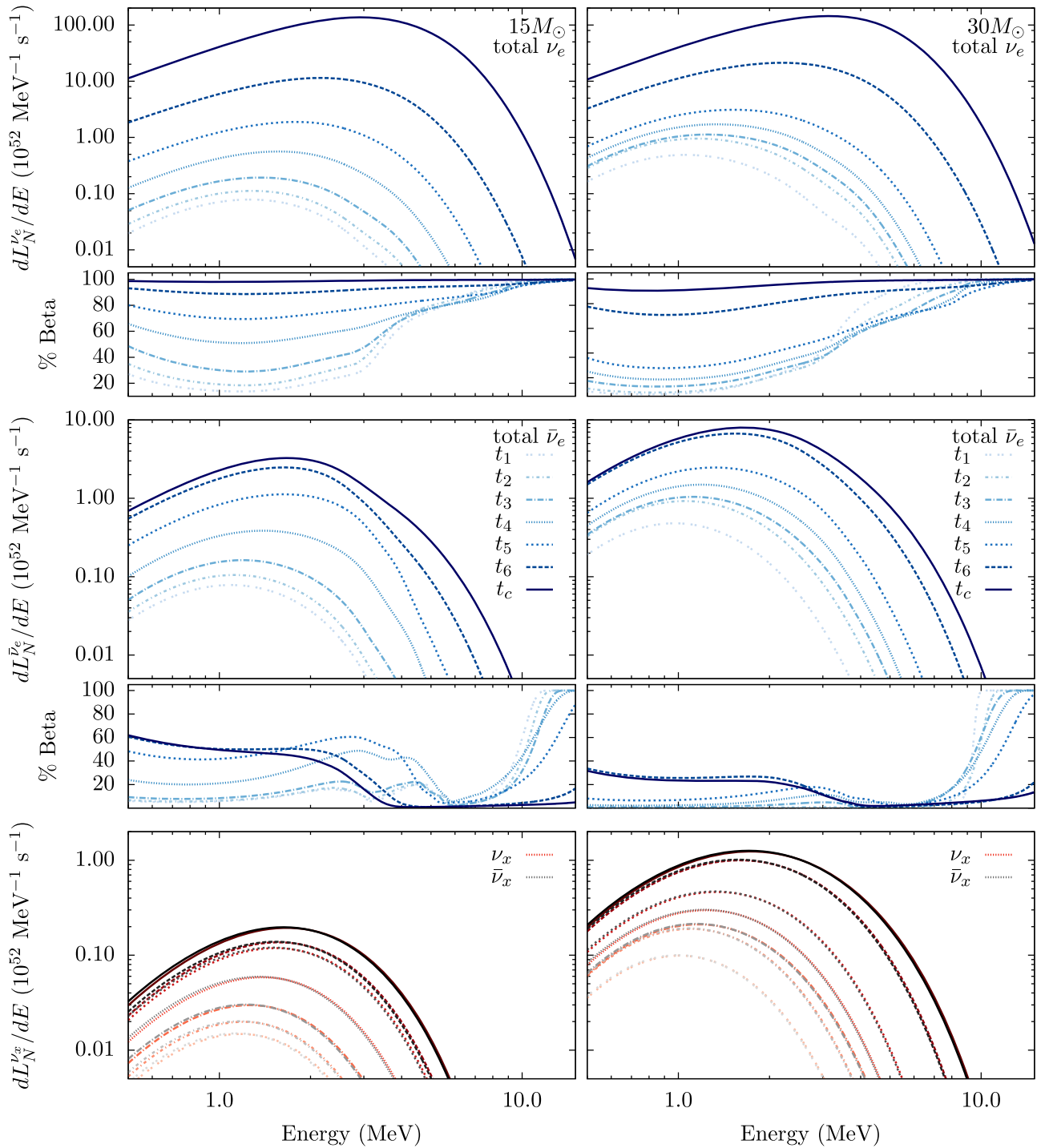
Figure 2. Neutrino spectra at selected times pre-collapse for a 15 $M_\odot$ star (left) and 30 $M_\odot$ star (right). Each set of curves shows times t_1 through t_c (lower to upper curves). The exact values of these times are given in Tables 1 and 2. The dashing styles in the legend apply to all panels. The first (third) panel shows the differential luminosity for electron (anti-)neutrinos. The second (fourth) panel shows the percentage of that luminosity arising from β processes. The bottom panel shows the $\nu_x/\bar{\nu}_x$ luminosity from pair annihilation.

the luminosity: the ν_e luminosity from the five dominant isotopes is between ~35%–45% for the total energy range, ending with ~50% at t_c. For $\bar{\nu}_e$, 78% of the luminosity is from the top-five isotopes at t_1. The percentage gradually decreases to 37% at t_c.

The results for the 30 $M_\odot$ model (Table 2) reflect its faster evolution. For this star, silicon shell-burning begins at $\tau \approx 5$ hr, therefore it is expected that at $\tau_{CC} \sim 2$ hr, there might still be a contribution from medium-mass nuclei. Indeed,

the largest contribution to the $\bar{\nu}_e$ luminosity at t_1 for the 30 $M_\odot$ star is from ^{28}Al. Subsequent times show the same pattern as the 15 $M_\odot$ model, with mainly isotopes with $A \approx 50$–60 dominating. We see that free protons appear in the top-five isotopes at $t_3 \approx 0.05$ hr ($\simeq 3$ minute) pre-collapse, and are the most dominant contributor from t_5 on. Free neutrons also appear in the top-five list for $\bar{\nu}_e$ above $E \geqslant 2$ MeV at t_c. For ν_e, the total contribution of the top-five isotopes is 66% at t_1, drops to about 40% later, then climbs again to end at 75% at t_c, of

Table 1
List of the Five Isotopes That Most Contribute to the Produced ν_e ($\bar{\nu}_e$) Presupernova Luminosity in the 15 $M_\odot$ Model—Total and at $E \geqslant 2$ MeV—at Selected Times

15 $M_\odot$											
τ_{CC} (hr)		ν_e							$\bar{\nu}_e$		
$t_1 = 2.038$	total	^{55}Fe	^{56}Fe	^{54}Fe	^{53}Fe	^{55}Co	^{56}Mn	^{57}Mn	^{55}Cr	^{52}V	^{53}V
		0.141	0.0846	0.0803	0.0778	0.0761	0.357	0.162	0.0937	0.0894	0.0817
	$E \geqslant 2$ MeV	^{53}Fe	^{55}Fe	^{55}Co	^{54}Mn	^{57}Ni	^{56}Mn	^{52}V	^{57}Mn	^{62}Co	^{55}Cr
		0.169	0.155	0.140	0.101	0.0393	0.423	0.107	0.0823	0.0729	0.0689
$t_2 = 1.086$	total	^{55}Fe	^{55}Co	^{56}Fe	^{53}Fe	^{54}Fe	^{56}Mn	^{57}Mn	^{55}Cr	^{52}V	^{53}V
		0.117	0.0860	0.0846	0.0805	0.0779	0.339	0.155	0.0937	0.0894	0.0767
	$E \geqslant 2$ MeV	^{53}Fe	^{55}Co	^{55}Fe	^{54}Mn	^{57}Ni	^{56}Mn	^{62}Co	^{52}V	^{57}Mn	^{58}Mn
		0.167	0.150	0.132	0.0923	0.0482	0.365	0.103	0.0940	0.0909	0.0848
$t_3 = 0.4793$	total	^{55}Fe	^{56}Fe	^{55}Co	^{54}Fe	^{53}Fe	^{56}Mn	^{57}Mn	^{55}Cr	^{53}V	^{52}V
		0.107	0.0973	0.0641	0.0610	0.0558	0.247	0.158	0.101	0.0761	0.0645
	$E \geqslant 2$ MeV	^{55}Fe	^{53}Fe	^{55}Co	^{54}Mn	^{57}Ni	^{56}Mn	^{58}Mn	^{57}Mn	^{55}Cr	^{62}Co
		0.132	0.115	0.106	0.0950	0.0424	0.236	0.125	0.116	0.0977	0.0957
$t_4 = 0.1022$	total	^{56}Fe	^{53}Cr	^{55}Fe	^{57}Fe	^{55}Mn	^{57}Mn	^{58}Mn	^{63}Co	^{55}Cr	^{56}Mn
		0.110	0.0839	0.0797	0.0554	0.0546	0.133	0.117	0.0981	0.0967	0.0930
	$E \geqslant 2$ MeV	^{55}Fe	^{54}Mn	^{56}Fe	^{53}Cr	^{55}Co	^{58}Mn	^{57}Mn	^{63}Co	^{55}Cr	^{62}Co
		0.104	0.0706	0.0685	0.0646	0.0486	0.166	0.107	0.101	0.0935	0.0812
$t_5 = 0.01292$	total	^{56}Fe	^{53}Cr	^{57}Fe	^{55}Fe	^{55}Mn	^{58}Mn	^{63}Co	^{57}Mn	^{62}Co	^{55}Cr
		0.0805	0.0783	0.0680	0.0603	0.0526	0.134	0.105	0.0844	0.0760	0.0700
	$E \geqslant 2$ MeV	^{55}Fe	^{53}Cr	^{54}Mn	^{56}Fe	^{57}Fe	^{58}Mn	^{63}Co	^{64}Co	^{62}Co	^{54}V
		0.0779	0.0678	0.0597	0.0553	0.0544	0.170	0.0953	0.0802	0.0695	0.0657
$t_6 = 1.632 \times 10^{-5}$	total	p	^{53}Cr	^{56}Fe	^{55}Mn	^{51}V	^{58}Mn	^{63}Co	^{57}Mn	^{55}Cr	^{54}V
		0.212	0.0761	0.0525	0.0497	0.0464	0.121	0.0889	0.0795	0.0691	0.0583
	$E \geqslant 2$ MeV	p	^{53}Cr	^{51}V	^{55}Mn	^{55}Fe	^{58}Mn	^{54}V	^{63}Co	^{55}Cr	^{59}Mn
		0.233	0.0726	0.0492	0.0459	0.0413	0.150	0.0869	0.0674	0.0600	0.0584
$t_7 = t_c$	total	p	^{53}Cr	^{55}Mn	^{51}V	^{57}Fe	^{58}Mn	^{54}V	^{57}Mn	^{55}Cr	^{56}Mn
		0.329	0.0565	0.0457	0.0414	0.0398	0.109	0.0838	0.0660	0.0639	0.0495
	$E \geqslant 2$ MeV	p	^{53}Cr	^{55}Mn	^{51}V	^{56}Mn	^{58}Mn	^{54}V	^{50}Sc	^{59}Mn	^{55}V
		0.353	0.0566	0.0441	0.0428	0.0387	0.123	0.113	0.0701	0.0686	0.0619

Note. The isotopes are listed in order of decreasing ν_e ($\bar{\nu}_e$) luminosity. The number below each isotope is the fraction of the βp number luminosity produced by that isotope.

which ~65% is from free protons. For $\bar{\nu}_e$, the total fraction is 85% at t_1, and gradually decreases to 40% at t_c.

The fact that, in both models, large portions of the ν_e and $\bar{\nu}_e$ luminosities come from a relatively small number of isotopes, is promising for future work: it means that efforts to produce more precise neutrino spectra could become more manageable, as they can be targeted to the subset of isotopes identified in Tables 1–2.

4. Propagation and Detectability

4.1. Oscillations of Presupernova Neutrinos

The flavor composition of the presupernova neutrino flux at Earth differs from the one at production, due to flavor conversion (oscillations). In terms of the original, unoscillated flavor luminosities, $F_\alpha^0 = dL_N^{\nu_\alpha}/dE$ ($\alpha = e, \bar{e}, x$), the fluxes of each neutrino species at Earth can be written as

$$F_e = pF_e^0 + (1-p)F_x^0 , \quad 2F_x = (1-p)F_e^0 + (1+p)F_x^0 , \quad (11)$$

where F_x is defined so that the total flux is $F_e + 2F_x = F_e^0 + 2F_x^0$, and the geometric factor $(4\pi D^2)^{-1}$, due to the distance D to the star, is omitted for brevity. An expression analogous to Equation (11) holds for anti-neutrinos, with the

notation replacements $e \to \bar{e}$ and $p \to \bar{p}$. The quantities p and $\bar{p}$ are the ν_e and $\bar{\nu}_e$ survival probabilities. They have been studied extensively for a supernova neutrino burst (see, e.g., (Duan & Kneller 2009) and references therein), and at a basic level for presupernova neutrinos (Kato et al. 2015, 2017; Asakura et al. 2016). Similar to the burst neutrinos, presupernova neutrinos undergo adiabatic, matter-driven conversion inside the star. The probabilities p and $\bar{p}$ are independent of energy and of time. They are given by the elements of the neutrino mixing matrix, $U_{\alpha i}$, in a way that depends on the (still unknown) neutrino mass hierarchy; given the masses m_i ($i = 1$–3), the standard convention defines the normal hierarchy (NH) as $m_3 > m_2$ and vice versa for the inverted hierarchy (IH). For each possibility, we have (see, e.g., Lunardini & Smirnov 2003; Kato et al. 2017):

$$p = \begin{cases} |U_{e3}|^2 \simeq 0.02 & \text{NH} \\ |U_{e2}|^2 \simeq 0.30 & \text{IH} \end{cases} \quad \bar{p} = \begin{cases} |U_{e1}|^2 \simeq 0.68 & \text{NH} \\ |U_{e3}|^2 \simeq 0.02 & \text{IH.} \end{cases} \quad (12)$$

For simplicity, here we do not consider other oscillation effects, namely collective oscillations inside the star and oscillations in the matter of the Earth. The former are expected to be negligible due to the relatively low presupernova neutrino luminosity (compared to the supernova burst), and the latter are

Table 2
Same as Table 1, but for the 30 $M_\odot$ Model

τ_{CC} (hr)		ν_e					$\bar{\nu}_e$				
$t_1 = 2.057$	total	^{54}Fe	^{55}Fe	^{55}Co	^{53}Fe	^{57}Co	^{28}Al	^{56}Mn	^{54}Mn	^{24}Na	^{27}Mg
		0.219	0.192	0.110	0.0913	0.0524	0.603	0.0890	0.0611	0.0557	0.0395
	$E \geqslant 2$ MeV	^{55}Fe	^{53}Fe	^{55}Co	^{54}Fe	^{56}Co	^{28}Al	^{24}Na	^{56}Mn	^{60}Co	^{23}Ne
		0.194	0.173	0.158	0.0798	0.0637	0.557	0.150	0.147	0.0532	0.0186
$t_2 = 0.4008$	total	^{56}Ni	^{55}Fe	^{55}Co	^{53}Fe	^{54}Fe	^{56}Mn	^{57}Mn	^{60}Co	^{61}Co	^{52}V
		0.282	0.107	0.0726	0.0629	0.0518	0.354	0.117	0.094	0.0597	0.0557
	$E \geqslant 2$ MeV	^{55}Fe	^{56}Ni	^{55}Co	^{53}Fe	^{52}Fe	^{56}Mn	^{57}Mn	^{60}Co	^{61}Co	^{55}Cr
		0.138	0.125	0.114	0.109	0.0606	0.383	0.119	0.0865	0.0623	0.0613
$t_3 = 0.05069$	total	^{55}Fe	^{56}Ni	^{56}Fe	p	^{55}Co	^{56}Mn	^{57}Mn	^{62}Co	^{55}Cr	^{58}Mn
		0.101	0.101	0.0782	0.0678	0.0472	0.229	0.126	0.0889	0.0799	0.0688
	$E \geqslant 2$ MeV	^{55}Fe	^{54}Mn	^{55}Co	p	^{56}Fe	^{56}Mn	^{57}Mn	^{62}Co	^{58}Mn	^{55}Cr
		0.128	0.0736	0.0621	0.0576	0.0540	0.207	0.119	0.109	0.0995	0.0883
$t_4 = 0.04892$	total	^{55}Fe	^{56}Ni	^{56}Fe	p	^{55}Co	^{56}Mn	^{57}Mn	^{62}Co	^{55}Cr	^{58}Mn
		0.101	0.101	0.0779	0.0698	0.0471	0.228	0.126	0.0870	0.0801	0.0683
	$E \geqslant 2$ MeV	^{55}Fe	^{54}Mn	^{55}Co	p	^{56}Fe	^{56}Mn	^{57}Mn	^{62}Co	^{58}Mn	^{55}Cr
		0.128	0.0736	0.0619	0.0595	0.0539	0.207	0.120	0.107	0.0990	0.0887
$t_5 = 0.00214$	total	p	^{55}Fe	^{56}Fe	^{56}Ni	^{54}Mn	^{58}Mn	^{57}Mn	^{56}Mn	^{62}Co	^{55}Cr
		0.284	0.0646	0.0532	0.0414	0.0363	0.116	0.109	0.107	0.0836	0.0829
	$E \geqslant 2$ MeV	p	^{55}Fe	^{54}Mn	^{56}Fe	^{57}Co	^{58}Mn	^{57}Mn	^{55}Cr	^{62}Co	^{56}Mn
		0.494	0.0442	0.0371	0.0281	0.0261	0.163	0.0917	0.0867	0.0794	0.0712
$t_6 = 0.0001142$	total	p	^{55}Fe	^{56}Fe	^{53}Cr	^{54}Mn	^{58}Mn	^{57}Mn	^{55}Cr	^{56}Mn	^{63}Cr
		0.487	0.0393	0.0371	0.0293	0.0283	0.121	0.0996	0.0809	0.0774	0.0645
	$E \geqslant 2$ MeV	p	^{55}Fe	^{54}Mn	^{56}Fe	^{53}Cr	^{58}Mn	^{54}V	^{55}Cr	^{57}Mn	^{63}Co
		0.494	0.0442	0.0371	0.0281	0.0261	0.167	0.0820	0.0811	0.0747	0.0576
$t_7 = t_c$	total	p	^{53}Cr	^{55}Mn	^{56}Fe	^{54}Mn	^{58}Mn	^{57}Mn	^{55}Cr	^{56}Mn	^{53}V
		0.639	0.0286	0.0252	0.0234	0.0213	0.0963	0.0943	0.0819	0.0747	0.0555
	$E \geqslant 2$ MeV	p	^{53}Cr	^{55}Mn	^{54}Mn	^{51}V	^{58}Mn	^{55}Cr	^{54}V	^{57}Mn	n
		0.659	0.0273	0.0236	0.0236	0.0212	0.124	0.0803	0.0760	0.0705	0.0638

suppressed (a ~1% effect or less) at the energies of interest here (see, e.g., Wan et al. 2017).

Equation (12) shows that for the NH, the ν_e flux at Earth receives only a very suppressed contribution from the original ν_e. The suppression is weaker for the IH, and therefore—considering that $F_x^0 \ll F_e^0$—the flux F_e should be much larger in this case. For the $\bar{\nu}_e$ flux, a smaller difference between NH and IH is expected, due to F_x^0 and $F_{\bar{e}}^0$ being comparable (Figure 1).

4.2. Window of Observability

A detailed discussion of the detectability of presupernova neutrinos is beyond the scope of this paper, and is deferred to future work. Here, general considerations are given for the region, in the time and energy domain, where detection might be possible—depending on the distance to the star—and the numbers of events expected in neutrino detectors are given.

One can define a conceptual window of observability (WO) as the interval of time and energy where the presupernova flux exceeds all the neutrino fluxes of other origin that are (i) present in a detector at all times, and (ii) indistinguishable from the signal. These fluxes are guaranteed backgrounds, regardless of the details of the detector in use; to them, detector-specific backgrounds will have to be added. Therefore, the WOs defined here represents a most optimistic, ideal situation.

Because observations at neutrino detectors are generally dominated by either ν_e or $\bar{\nu}_e$, let us discuss the WOs for these two species. In the case of ν_e, the largest competing flux is due to solar neutrinos (Bahcall et al. 2005). For $\bar{\nu}_e$, we consider fluxes from nuclear reactors and from the Earth's natural radioactivity (geoneutrinos; Fiorentini et al. 2007). For both ν_e and $\bar{\nu}_e$, other background fluxes are from atmospheric neutrinos and from the diffuse supernova neutrino background (DSNB, due to all the supernova neutrino bursts in the universe). At the times and energies of interest, however, these are much lower than the solar, reactor, geoneutrinos, and presupernova fluxes, and therefore they will be neglected from here on.

The reactor neutrino and geoneutrino spectra depend on the location of the detector in relation to working reactors and local geography. The reactor spectrum we use was calculated for the Pyhäsalmi mine in Finland (Wurm 2009; Mollenberg et al. 2015), and includes oscillations. The geoneutrino spectrum is generic, and includes vacuum oscillations only, with the survival probability at JUNO $\bar{p} \simeq 0.55$ for both NH and IH (Wan et al. 2017).[8]

Figures 4 and 5 show the presupernova neutrino signal at Earth for a star at $D = 1$ kpc. It appears that, already two hours before collapse, the presupernova ν_e flux emerges above solar neutrinos. The WO becomes wider in energy as the

---

[8] Effects from MSW oscillation are shown to be at the level of 0.3% (Wan et al. 2017), and therefore can be neglected.
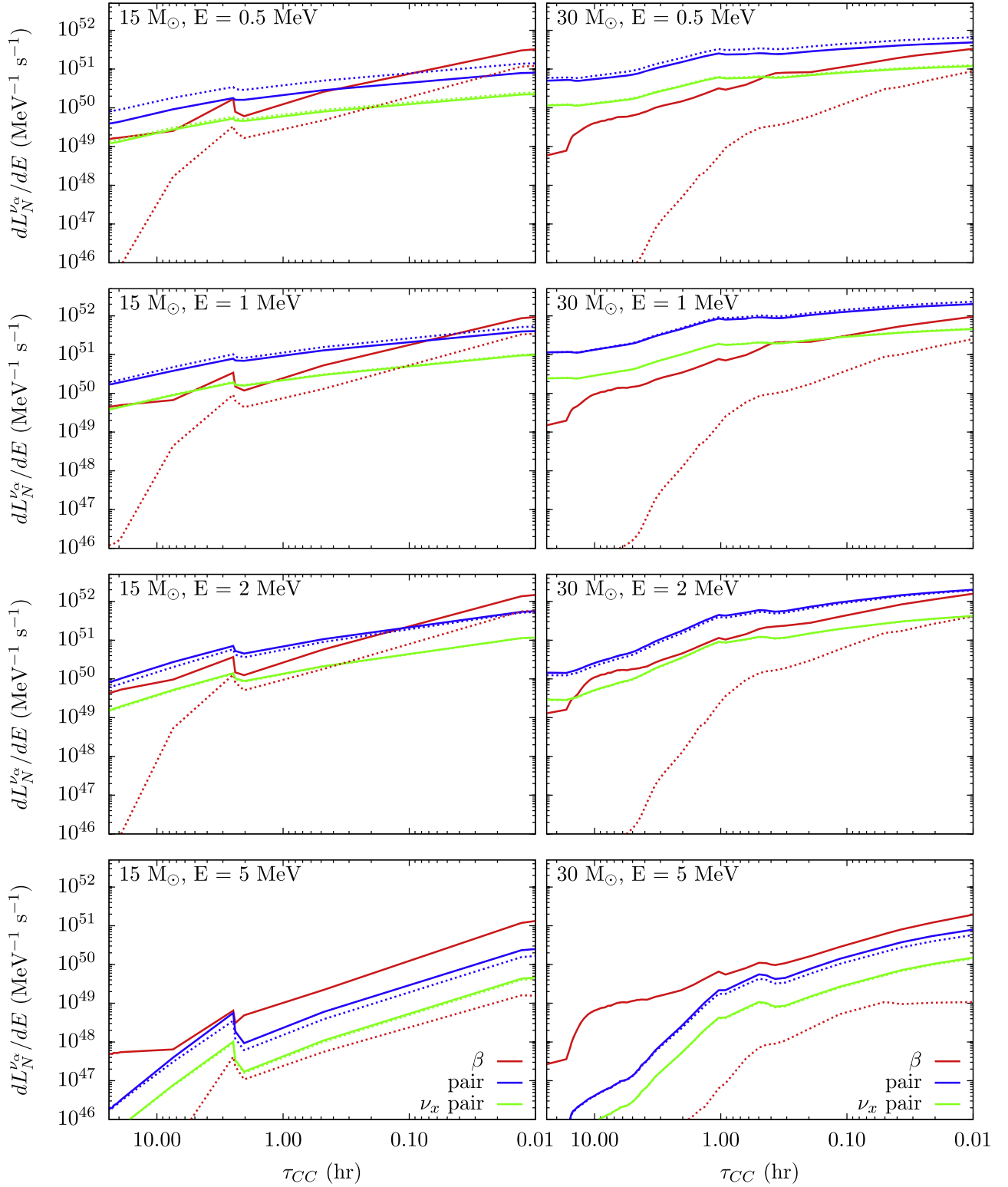
Figure 3. Time evolution of the neutrino luminosity for a 15 $M_\odot$ star (left) and a 30 $M_\odot$ star (right), differential in energy, at selected energies. The contributions of the thermal and beta processes are shown separately. The solid lines represent neutrinos, while the dashed lines show the anti-neutrino contributions.

presupernova flux increases with time. An approximate WO is $\tau_{CC} \sim$ 0–2 hr, and $E \sim$ 1–8 MeV, and it is larger for the IH and for the more massive progenitor, where the presupernova flux is higher. We note that it may be possible to distinguish and subtract solar neutrinos effectively using their arrival direction, e.g., in neutrino-electron scattering events in water

Cherenkov detectors (Abe et al. 2011b). With a $\sim 10^4$ reduction in the solar background, the ν_e WO would extend in energy and time, $\tau_{CC} \sim$ 0–24 hr, and $E \sim$ 0.5–10 MeV.

For the same distance $D = 1$ kpc, the WO for $\bar{\nu}_e$ is similar to that of ν_e, but it is overall wider in energy, as the presupernova flux eventually exceeds the geoneutrino flux at sub-MeV
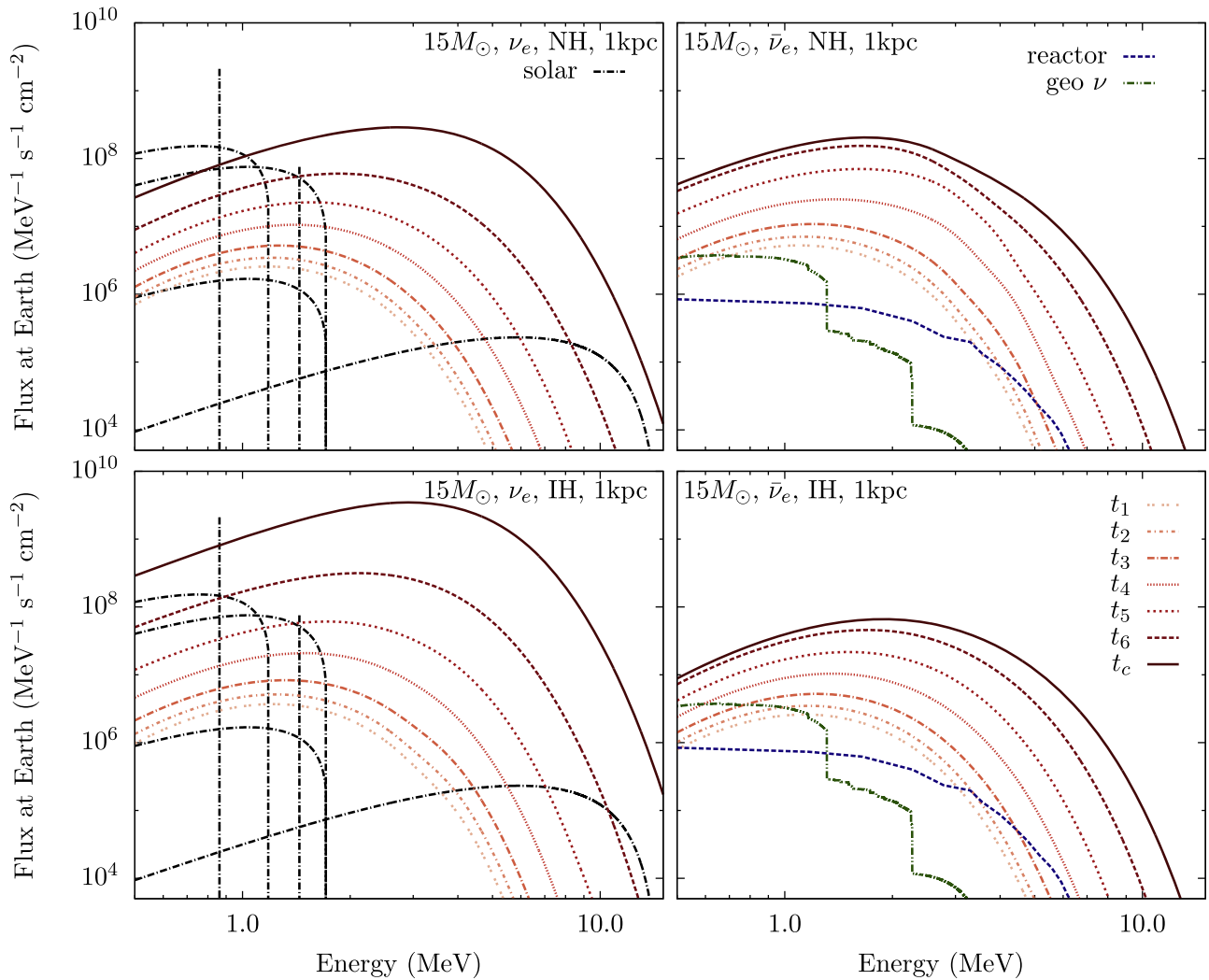
Figure 4. Fluxes of ν_e (left panels) and $\bar{\nu}_e$ (right panels) expected at Earth from a 15 $M_\odot$ star at distance $D = 1$ kpc, calculated at times t_1 through t_c (lower to upper curves). Shown are the cases of normal and inverted mass hierarchy (upper and lower rows, respectively). Competing neutrino fluxes from other sources are shown (see the legend). Oscillations are included in all cases.

energy. Approximately, the WO is $\tau_{CC} \sim 0$–2 hr, and $E \sim$ 0.5–20 MeV.

By increasing the distance D, the WO becomes narrower; unless the background fluxes in Figures 4 and 5 are subtracted, it eventually closes completely for $D \sim 30$ kpc. This maximum distance—which is of the order of the size our galaxy—is independent of the specific detector considered. We will see below that the actual horizon for observation is smaller for realistic detector masses.

It is possible that the next supernova in our galaxy will be closer than 1 kpc, thus offering better chances of presupernova neutrino observation. A prime example is the red supergiant Betelgeuse (α Orionis). Betelgeuse has the largest angular diameter on the sky of any star apart from the Sun, and is the ninth-brightest star in the night sky. As such, it has been well-studied. Betelgeuse is estimated to have a mass of 11–20 $M_\odot$ (Lobel & Dupree 2001; Neilson et al. 2011; Dolan et al. 2016; Neilson et al. 2016); it lies at a distance of 222^{+48}_{-34} pc (Harper et al. 2008, 2017), and has an age of 8–10 Myr, with <1 Myr of life left until core collapse (Dolan et al. 2016; Harper et al. 2017). We find that for $D = 200$ pc, a presupernova neutrino signal would be practically background-free—in

energy windows that are realistic for detection—for several hours, and the WO can extend up to $\sim$10 hr.

4.3. Numbers of Events, Horizon

Let us now briefly discuss the expected numbers of events at current and near-future detectors of $\mathcal{O}(10)$ kt scale or higher. We consider the three main detection technologies: liquid scintillator (LS; JUNO An et al. 2016), water Cherenkov (SuperKamiokande; Abe et al. 2014) and liquid argon (DUNE; Bishai et al. 2015). For each, we consider the dominant detection channel—that will account for the majority of the events in the detector—and the first subdominant process that is sensitive to ν_e. The latter will be especially sensitive to ν_e from the βp.

For water Cherenkov and LS, the dominant detection process is inverse beta decay (IBD), $\bar{\nu}_e + p \rightarrow n + e^+$, which bears some sensitivity to $\bar{\nu}_e$ from βp. The sensitivity to ν_e from the βp is in the subdominant channel, neutrino-electron elastic scattering (ES), where the contribution of ν_e is enhanced (compared to ν_x) by the larger cross section. Note that the two channels, IBD and ES, can be distinguished in the detector, at least in part, due to their different final state signatures:
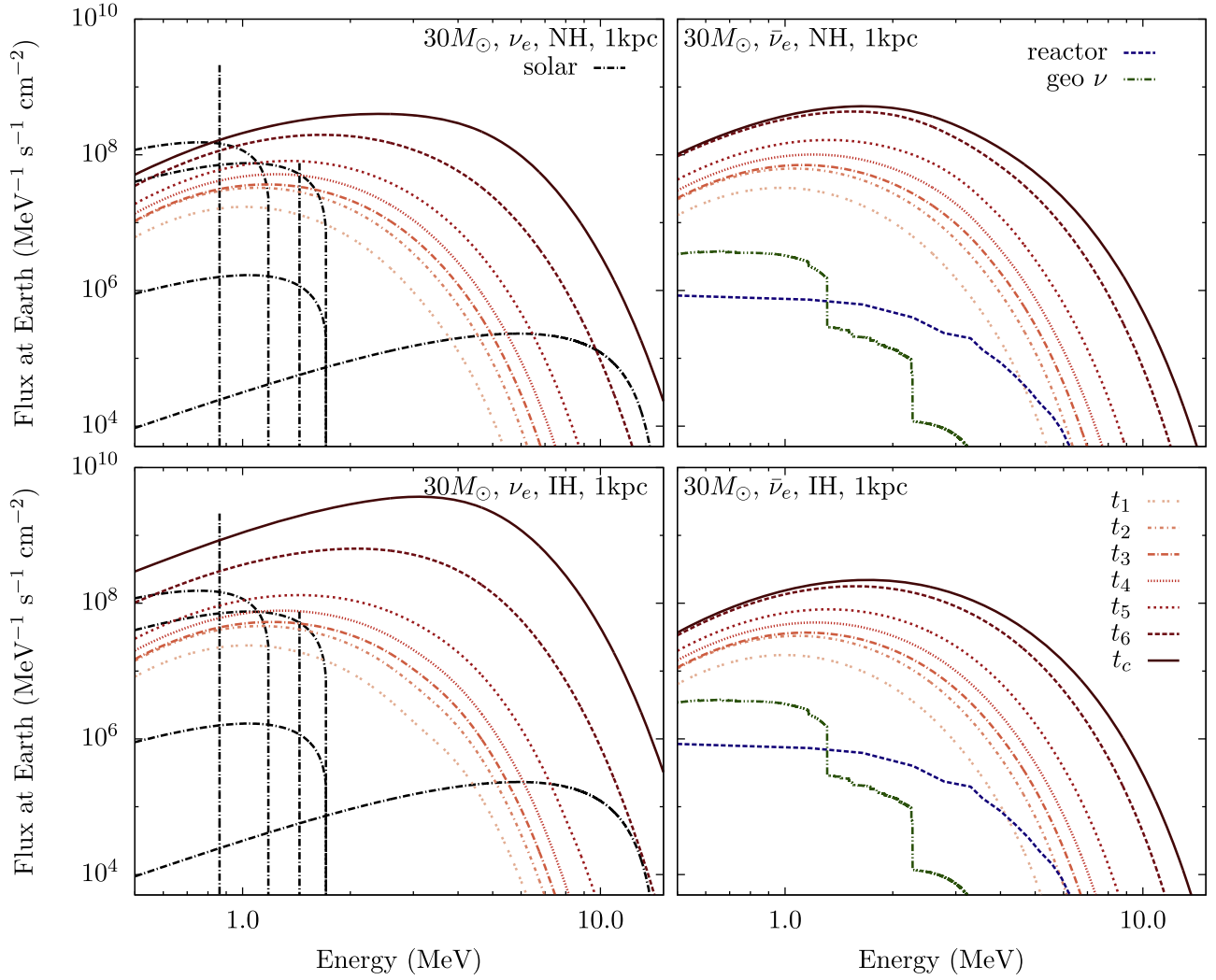
Figure 5. Same as Figure 4, but for a 30 $M_\odot$ star.

Table 3
Numbers of Events Expected in the Two Hours Prior to Collapse, for a Presupernova with Progenitor Mass $M = 15\,M_\odot$, at Distance $D = 1$ kpc and the Normal Mass Hierarchy

Detector	Composition	Mass	Interval	N_β^{CC}	N_β^{el}	N^{CC}	N^{el}	$N^{tot} = N^{CC} + N^{el}$
JUNO	C_nH_{2n}	17 kt	$E_e \geqslant 0.5$ MeV	3.19 [0.09]	2.34 [4.32]	10.1 [2.592]	7.19 [10.2]	17.3 [12.8]
SuperKamiokande	H_2O	22.5 kt	$E_e \geqslant 4.5$ MeV	0.04 [0.00]	0.02 [0.05]	0.43 [0.15]	0.03 [0.06]	0.45 [0.21]
DUNE	LAr	40 kt	$E \geqslant 5$ MeV	0.017 [0.27]	0.013 [0.032]	0.046 [0.33]	0.018 [0.039]	0.063 [0.37]

Note. The numbers in brackets refer to the inverted mass hierarchy. Different columns give the numbers for different detection channels: the superscripts CC and el refer, respectively, to the dominant charged current process (inverse beta decay or ν_e absorption on the Ar nucleus) and to neutrino-electron scattering. The subscript β indicates the contribution of the β processes to those two channels. The total number of events is given in the last column. The results for Betelgeuse ($D = 0.2$ kpc) can be obtained by rescaling by a factor of 25.

neutron-capture in coincidence for IBD, and the peaked angular distribution for ES (see, e.g., Beacom & Vogel 1999; Ando & Sato 2002). In SuperKamiokande, efficient neutron-capture will be possible in the upcoming upgrade with Gadolinium addition (Beacom & Vagins 2004).

In LS, the main detection processes are the same as in water, with the differences being that LS offers little directional sensitivity but has the advantage of a lower, sub-MeV energy threshold, which can capture most of the presupernova spectrum.

In liquid argon (LAr), the dominant process is ν_e charged current-scattering on the argon nucleus. Therefore, LAr is, in principle, extremely sensitive to neutrinos from the βp. However, the relatively high energy threshold ($E_{th} \sim 5$ MeV)

Table 4
Same as Table 3, but for the $M = 30\,M_\odot$ Progenitor

Detector	Composition	Mass	Interval	N_β^{CC}	N_β^{el}	N^{CC}	N^{el}	$N^{tot} = N^{CC} + N^{el}$
JUNO	C_nH_{2n}	17 kt	$E_e \geqslant 0.5$ MeV	1.83	4.40	40.1	32.1	72.3
				[0.05]	[9.47]	[13.1]	[42.7]	[55.9]
SuperKamiokande	H_2O	22.5 kt	$E_e \geqslant 4.5$ MeV	0.063	0.053	2.27	0.098	2.37
				[0.00]	[0.13]	[0.78]	[0.20]	[0.98]
DUNE	LAr	40 kt	$E \geqslant 5$ MeV	0.05	0.04	0.19	0.06	0.25
				[0.76]	[0.09]	[1.1]	[0.13]	[1.2]

Acciarri et al. 2015) is a considerable disadvantage compared to LS.

Tables 3 and 4 summarize our results for the number of presupernova neutrino events expected above realistic thresholds during the last two hours, pre-collapse. The numbers of background events are not given because they are affected by large uncertainties on the contributions of detector-specific backgrounds. These ultimately depend on the type of search performed, and have not been studied in detail yet for a presupernova signal.[9]

The tables confirm that a large LS like JUNO has the best potential, due to its sensitivity at low energy, with $N \sim 10\text{--}70$ events (depending on the type of progenitor) recorded from a star at $D = 1$ kpc. For these events, the contribution of the βp is at the level of 10%–30%, and is larger for the inverted mass hierarchy, for which the ν_e flux is larger; see Section 4.1. For Betelgeuse, a spectacular signal of more than 200 events in two hours could be seen. One can define (optimistically) the horizon of the detector, D_h, as the distance for which one signal event is expected. We find that JUNO has a horizon $D_h \sim 2\text{--}8$ kpc.

Although it is disadvantaged by the higher energy threshold, SuperKamiokande and DUNE can observe presupernova neutrinos for the closest stars. For the most massive progenitor, SuperKamiokande could reach a horizon $D_h \sim 1$ kpc; and record $N \sim 5\text{--}60$ events for $D = 0.2$ pc. Of these, $\sim$10%–20% would be from βp. Looking further into the future, the larger water Cherenkov detector HyperKamiokande (Abe et al. 2011a)—with a mass 20 times the mass of Super-Kamiokande—might become a reality. Assuming an identical performance as SuperKamiokande, HyperKamiokande will have a statistics of up to thousands of events, and a horizon of $\sim$4–5 kpc.[10]

At DUNE, a detection is possible only for the closest stars; the number of events varies between $N \sim 1$ and $N \sim 30$, depending on the parameters, for $D = 0.2$ kpc. For the most optimistic scenario (the more massive progenitor and the inverted mass hierarchy), the horizon can reach $D_h \sim 1$ kpc. DUNE will observe a strong component due to βp, at the level of $\sim$40%–80% of the total signal. Therefore, in principle LAr has the best capability to probe the isotopic evolution of supernova progenitors.

---

[9] Most background rejection studies have been performed for types of signals that are either constant in time or very short (e.g., a supernova burst). A presupernova signal is intermediate, rising steadily over a timescale of hours. This feature might require developing different approaches to cut backgrounds.

[10] Due to its mass, HyperKamiokande will have a level of background that is $\sim$20 times higher than that of SuperKamiokande, and probably a higher energy threshold as well. Therefore, its performance will be worse, and the figures given here have to be taken as best case scenarios.

5. Discussion

We have presented a new calculation of the total neutrino flux from beta processes in a presupernova star, inclusive of time-dependent emissivities and neutrino energy spectra. This is part of a complete and detailed calculation of presupernova neutrino fluxes from most relevant processes—beta and thermal—done using the state-of-the-art stellar evolution code MESA.

The beta neutrino flux is strongest in the ν_e channel, where it is comparable to the flux from thermal processes in the few hours pre-collapse, and it even exceeds it in the high-energy tail of the spectrum, $E \gtrsim 3$ MeV. This is very relevant for current and near-future detectors, which are most sensitive above the MeV scale.

Among the realistic detection technologies, LS is best suited to detect presupernova neutrinos. This is due to its lower energy threshold, which allows capture of the bulk of the flux hours or minutes before collapse. In such detector neutrinos from beta processes would contribute up to $\sim$30% of the total number of events, for a threshold of $\sim$0.5 MeV. The horizon for detection (i.e., the distance from the star where a few events are expected in the detector) is a few kpc for a 17 kt detector, with tens of events expected for $D \simeq 1$ kpc. The number of events increases strongly with the mass of the progenitor star; therefore, for medium-high statistics and known D, the presupernova neutrino signal will contribute to establishing the type of progenitor. For high statistics, the time profile of the presupernova signal could provide additional information, e.g., on the time of ignition of the different fuels (Figure 1).

At water Cherenkov and liquid Argon detectors of realistic sizes and thresholds ($E_{th} \sim 4\text{--}5$ MeV), the horizon is generally limited to the closest stars, $D \sim \mathcal{O}(0.1)$ kpc, but could reach 1 kpc for the most massive progenitors and the inverted neutrino mass hierarchy. For liquid argon, the contribution of the β neutrinos is strong, and could even dominate the signal. Therefore—at least in principle—liquid Argon detectors offer the possibility of probing the complex nuclear processes in stellar cores.

If the high-energy tail of a presupernova flux is detected, what nuclei and what processes exactly can we probe? To answer this question, we have identified the isotopes that contribute the most to the presupernova ν_e flux in the detectable energy window, which are generally iron, manganese, and cobalt isotopes, as well as free protons and neutrons. The possibility that neutrino detectors may test the physics of these isotopes is completely novel.

In closing, we stress that our calculation used the best available instruments: a state-of-the-art stellar evolution code, combined with the most up-to-date studies of nuclear rates and

beta spectra. Still, these instruments are affected by uncertainties, which naturally affect the results in this paper. In particular, while total emissivities are relatively robust, it is likely that the highest-energy tails of the neutrino spectrum, in the detectable window, are very sensitive to the details of the calculation, i.e., the temperature profile of the star, the nuclear abundances and the quantities in the nuclear tables we have used. Specifically, for neutrino spectra, a source of error lies in the single-strength approximation that is adopted here for βp (Section 2). A recent paper (Misch & Fuller 2016) presents an exploratory study of this error and concludes that while the single effective Q-value approach results in the correct emissivity and average energy, the specific energy spectrum could miss important features. A systematic extension of this result to the many isotopes included in MESA would be highly desirable to improve our results. Another interesting addition to the code would be the contribution of neutrino pair production via neutral current de-excitation (Misch & Fuller 2016), which is currently omitted in MESA. This de-excitation results in higher-energy neutrino spectra than the processes described in this work, and thus makes detections more likely.

Until these important improvements become available, our results have to be interpreted conservatively, as proof of the possibility that current and near-future detectors might be able to observe presupernova neutrinos, and therefore offer the first, *direct* test of the isotopic evolution of a star in the advanced stages of nuclear burning.

ORCID iDs

Kelly M. Patton ⓘ https://orcid.org/0000-0002-2154-4782
Cecilia Lunardini ⓘ https://orcid.org/0000-0002-9253-1663
Robert J. Farmer ⓘ https://orcid.org/0000-0003-3441-7624
F. X. Timmes ⓘ https://orcid.org/0000-0002-0474-159X

References

Abe, K., Abe, T., Aihara, H., et al. 2011a, arXiv:1109.3262
Abe, K., Hayato, Y., Iida, T., et al. 2011b, PhRvD, 83, 052010
Abe, K., Hayato, Y., Iida, T., Iyogi, K., et al. 2014, NIMPA, 737, 253
Acciarri, R., Acero, M. A., Adamowski, M., et al. 2015, arXiv:1512.06148
An, F., An, G., An, Q., et al. 2016, JPhG, 43, 030401
Ando, S., & Sato, K. 2002, PThPh, 107, 957
Asakura, K., Gando, A., Gando, Y., et al. 2016, ApJ, 818, 91
Bahcall, J. N., Serenelli, A. M., & Basu, S. 2005, ApJL, 621, L85
Beacom, J. F., & Vagins, M. R. 2004, PhRvL, 93, 171101
Beacom, J. F., & Vogel, P. 1999, PhRvD, 60, 033007
Bishai, M., McCluskey, E., Rubbia, A., & Thomson, M. 2015, Long-Baseline Neutrino Facility (LBNF) and Deep Underground Neutrino Experiment (DUNE) Conceptual Design Report, Vol. 1 (Washington, DC: US Depart. Energy), http://lbne2-docdb.fnal.gov/cgi-bin/ShowDocument?docid=10687
Dolan, M. M., Mathews, G. J., Lam, D. D., et al. 2016, ApJ, 819, 7
Duan, H., & Kneller, J. P. 2009, JPhG, 36, 113201
Dutta, S. I., Ratkovic, S., & Prakash, M. 2004, PhRvD, 69, 023005
Farmer, R., Fields, C. E., Petermann, I., et al. 2016, ApJS, 227, 22
Fiorentini, G., Lissia, M., & Mantovani, F. 2007, PhR, 453, 117
Fuller, G. M., Fowler, W. A., & Newman, M. J. 1980, ApJS, 142, 447
Fuller, G. M., Fowler, W. A., & Newman, M. J. 1982a, ApJ, 252, 715
Fuller, G. M., Fowler, W. A., & Newman, M. J. 1982b, ApJS, 48, 279
Fuller, G. M., Fowler, W. A., & Newman, M. J. 1985, ApJ, 293, 1
Harper, G. M., Brown, A., & Guinan, E. F. 2008, AJ, 135, 1430
Harper, G. M., Brown, A., Guinan, E. F., et al. 2017, AJ, 154, 11
Itoh, N., Hayashi, H., Nishikawa, A., & Kohyama, Y. 1996, ApJS, 102, 411
Kato, C., Azari, M. D., Yamada, S., et al. 2015, ApJ, 808, 168
Kato, C., Yamada, S., Nagakura, H., et al. 2017, ApJ, 848, 48
Koura, H., Tachibana, T., Uno, M., & Yamada, M. 2003, RIKEN Accel Prog., 36, 9
Koura, H., Tachibana, T., Uno, M., & Yamada, M. 2005, PThPh, 113, 305
Kutschera, M., Odrzywolek, A., & Misiaszek, M. 2009, AcPPB, 40, 3063
Langanke, K., Martinez-Pinedo, G., & Sampaio, J. M. 2001, PhRvC, 64, 055801
Lobel, A., & Dupree, A. K. 2001, ApJ, 558, 815
Lunardini, C., & Smirnov, A. Y. 2003, JCAP, 0306, 009
Misch, G. W., & Fuller, G. M. 2016, PhRvC, 94, 055808
Misiaszek, M., Odrzywolek, A., & Kutschera, M. 2006, PhRvD, 74, 043006
Mollenberg, R., von Feilitzsch, F., Hellgartner, D., et al. 2015, PhRvD, 91, 032005
Neilson, H. R., Baron, F., Norris, R., Kloppenborg, B., & Lester, J. B. 2016, ApJ, 830, 103
Neilson, H. R., Lester, J. B., & Haubois, X. 2011, in ASP Conf. Ser. 451, 9th Pacific Rim Conference on Stellar Astrophysics, ed. S. Qain et al. (San Francisco, CA: ASP), 117
Oda, T., Hino, M., Muto, K., Takahara, M., & Sato, K. 1994, ADNDT, 56, 231
Odrzywolek, A. 2007, EPJC, C52, 425
Odrzywolek, A. 2009, PhRvC, 80, 045801
Odrzywolek, A., & Heger, A. 2010, AcPPB, B41, 1611
Odrzywolek, A., Misiaszek, M., & Kutschera, M. 2004a, APh, 21, 303
Odrzywolek, A., Misiaszek, M., & Kutschera, M. 2004b, AcPPB, 35, 1981
Patton, K. M., Lunardini, C., & Farmer, R. J. 2017, ApJ, 840, 2
Paxton, B., Bildsten, L., Dotter, A., et al. 2011, ApJS, 192, 3
Paxton, B., Cantiello, M., Arras, P., et al. 2013, ApJS, 208, 4
Paxton, B., Marchant, P., Schwab, J., et al. 2015, ApJS, 220, 15
Ratkovic, S., Dutta, S. I., & Prakash, M. 2003, PhRvD, 67, 123002
Tachibana, T. 2000, RIKEN Rev., 26, 109
Tachibana, T., & Yamada, M. 1995, in Proc. Inc. Conf. on Exotic Nuclei and Atomic Masses, ed. M. de Saint Simon & O. Sorlin (Gif-sur-Yvette: Ed. Frontières), 763
Timmes, F. X., Woosley, S. E., & Weaver, T. A. 1996, ApJ, 457, 834
Wan, L., Hussain, G., Wang, Z., & Chen, S. 2017, PhRvD, 95, 053001
Weaver, T. A., & Woosley, S. E. 1993, PhR, 227, 65
Woosley, S. E., Heger, A., & Weaver, T. A. 2002, RvMP, 74, 1015
Wurm, M. 2009, PhD thesis, Technische Univ. München
Yoshida, T., & Tachibana, T. 2000, JNST, 37
Yoshida, T., Takahashi, K., Umeda, H., & Ishidoshiro, K. 2016, PhRvD, 93, 123012